Magnetic Field Modeling in High-Current Multiwire Submerged Arc Welding of Steel Pipes

Research of magnetic force between magnetized steel pipes and long cantilever welding torches in oil and gas pipe multiwire SAW

BY Y. ZHOU, Z. YANG, K. GUAN, B. CHANG, AND D. DU

Abstract

Multiwire submerged arc welding (MSAW) is an efficient joining technology widely used in manufacturing large-diameter oil and gas steel pipes. During spiral pipe MSAW, the long cantilever welding torch (LCWT) for inner welding is prone to vibration due to the magnetic effects from high welding currents, which decreases welding stability. This paper studies the magnetic field for the internal welding scenario in spiral pipes using a combination of experimental measurements and finite element methods. Welding experiments were performed on spiral pipe MSAW equipment, and the influence of the magnetized steel pipe was investigated. Finite element methods were then performed to simulate magnetic field distribution and the electromagnetic loads on the LCWT. Finally, the response of the LCWT to electromagnetic loads was computed using an analytical method. Based on magnetic field modeling, this study reveals the magnetization of steel pipes and its influence on magnetic distribution. Further, it confirms that the vibrations of LCWT are due to the electromagnetic load from the magnetized steel pipe. This study identifies the physical mechanism of torch vibration under electromagnetic excitation, providing a basis for designing stable and efficient spiral pipe final-welding systems.

https://doi.org/10.29391/2025.104.019

Keywords

- Magnetic Field Modeling
- High-Current Welding
- Multiwire Submerged Arc Welding
- Oil And Gas Steel Pipe
- Magnetic Force

Introduction

The increasing demand for pipeline transportation in the oil and gas industry is shifting toward steel pipes with higher grades, larger diameters, and thicker walls (Refs. 1–3), posing challenges for pipe production techniques and equipment (Ref. 4). To enhance efficiency, multiwire submerged arc welding (MSAW) (Refs. 5, 6), an evolution from traditional single-wire submerged arc welding (SAW) (Ref. 7), has become the dominant welding technology in oil and gas steel pipe manufacturing (Ref. 8). MSAW technology in oil and gas steel pipe manufacturing typically arranges two to five welding wires in a row to form a single shared weld pool, with each wire powered separately. The first wire is powered by direct current (DC) to ensure sufficient penetration, while the subsequent wires are powered with alternating current (AC) (Ref. 9), and the total current applied may reach thousands of amperes (Ref. 10).

Oil and gas steel pipeline construction primarily employs longitudinal submerged arc-welded (LSAW) and spiral submerged arc-welded (SSAW) pipes (Refs. 11, 12). Compared to LSAW pipes, SSAW pipes offer benefits such as lower production costs and enhanced flexibility, gaining increasing recognition in the industry. Currently, the manufacture of large-diameter and thick-walled SSAW pipes follows a process referred to as "two-step" (Refs. 13, 14), as illustrated in Fig. 1. First, the steel strip is wound spirally into a cylinder shape on a forming machine, with continuous gas metal arc welding (GMAW) employed to join the strip edges.

A plasma cutter cuts the tack-welded pipe into segments with the required length. Second, the pipe segments are transported to separate final-welding production lines and undergo double-sided MSAW. Because the pipe lengths often exceed 10 m, the welding machine is mounted on the end of a long cantilever to form a long cantilever welding torch (LCWT) for internal welding.

MSAW involves more arcs, higher current, and a more complex welding process than traditional single-arc welding, which presents significant technical challenges to the welding procedure. The multiple arcs in MSAW are prone to deflection, distortion, and even extinguishment, thus affecting weld quality (Refs. 15, 16). Research has been conducted on the arc interaction and stability in MSAW. Kozuki et al. (Ref. 4) investigated arc behavior during the four-wire SAW process of UOE steel pipes. They thinned the flux layer to expose the arc, enabling direct observation of arc behaviors. Cho et al. (Ref. 17) established an MSAW process model and analyzed the weld pool's behavior using an arc interaction model under different current values. Kiran (Ref. 18) studied arc behavior in double-wire SAW and developed equations to predict arc interactions for various welding parameters. They investigated arc oscillation in three-wire SAW and developed a model to estimate arc center displacement.

In addition to multiple arc interactions, the complexity of MSAW is augmented by the magnetic effects of high welding currents. Research has demonstrated the existence of a low-frequency magnetic field near the welding cable, induced by the welding current, which is typically considered insignificant in welding manufacturing (Refs. 19, 20). However, in MSAW, the much higher current results in non-negligible electromagnetic effects on welding equipment and steel pipe. In spiral pipe MSAW procedures, it has been observed that the LCWT is prone to low-frequency vertical vibration due to magnetic forces. The oscillation of the welding machine disturbs the arc length and affects the stability of the arc welding process, thus decreasing the SSAW quality. This issue has been a primary concern in the steel pipe manufacturing industry. However, there is no clear understanding regarding the mechanism by which the magnetic field leads to the vibration of the LCWT during pipe MSAW. Furthermore, few attempts have been made to investigate the magnetic effects of welding circuit currents in MSAW and the impact on pipe production.

Motivated by the limitation of current research, this study developed a magnetic field model for the inner welding process of MSA-welded pipes by combining welding experiments with finite element (FE) method simulations, investigating the spatial distribution of the magnetic field and the effects of steel pipe magnetization. Based on simulations, the electromagnetic loads on the LCWT were calculated, and the responses of the LCWT were analyzed, revealing the vibration mechanism of the LCWT in MSAW of spiral steel pipes.

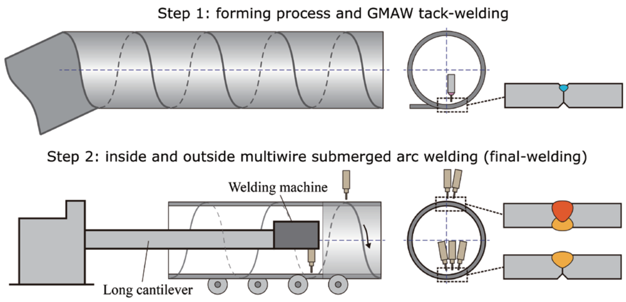

Fig. 1 — Schematic diagram of the two-step process for SSAW pipe welding.

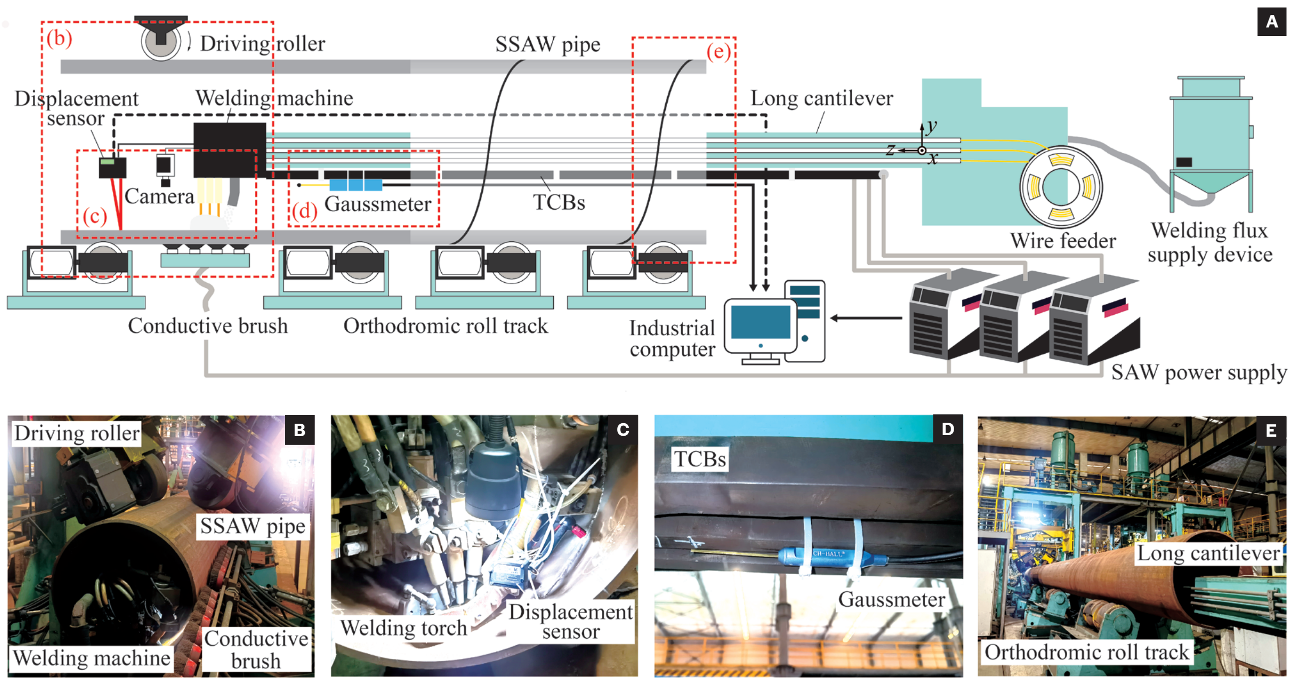

Fig. 2 — Welding equipment: A — Production line schematic; B–E — show the partial details of the equipment.

Method

Welding Experiment Procedures

Welding experiments were conducted based on a spiral pipe MSAW production line, as depicted in Fig. 2. The production line consisted primarily of a driving transmission system, a welding system, a vision tracking system, and a flux supply and recovery system. The driving transmission system, composed mainly of orthogonal roll tracks and driving rollers, was designed to propel the pipe segment in axial movement and circumferential rotation. The welding system comprised multiple SAW power supplies, an automatic wire feed mechanism, and a uniform cross-section 20-meter-long cantilever with a welding machine mounted at its end. The welding machine integrated three welding torches, each independently powered by a power source (Power Wave® AC/DC 1000 SD) via transmission copper busbars (TCBs) fixed on the cantilever.

Measurement devices were integrated into pipe welding equipment, including a laser displacement sensor (Keyence IL-065), a one-dimensional gaussmeter (CH-1600), and power monitors. As shown in Fig. 2C, the laser displacement sensor was affixed to the welding machine to measure the distance between the welding machine and the steel pipe. The distance served as a proxy for the displacement of the LCWT, given the minor transverse movement of the pipe during the welding process. As shown in Fig. 2D, the gaussmeter was mounted on the cantilever to measure the magnetic flux density at a designated point in space. The power monitor was used to record the output voltage, current of the power source, and wire feed speed. These measurement devices were interfaced with an industrial computer to facilitate real-time data transmission.

The driving transmission system first transported the pipe to the initial welding position during the welding experiment. Flux was then applied to the weld joint, after which the welding machine was activated to initiate the arc and weld along the joint, guided by the vision tracking system. The driving roller drove the helical movement of the pipe along the orthogonal

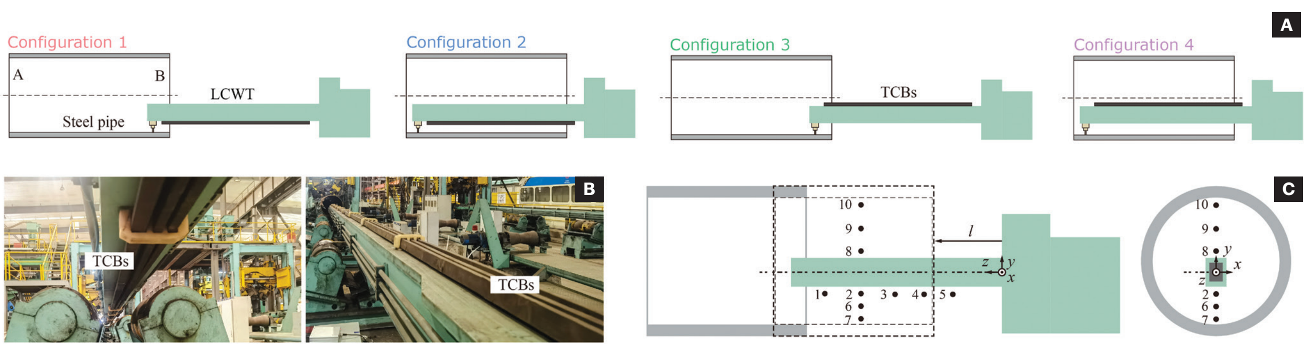

Fig. 3 — Schematic diagram of four welding configurations and measurement point distribution: A — Four welding configurations; B — TCB fixing position; C — measurement point distributions.

Table 1 — Welding Experiment Parameters

Wire	Size	Wire Grade	Current	Voltage	Power Polarity	Frequency
1	Φ 4.0 mm	CHW-GX6	850 A	32 V	DC+	–
2	Φ 4.0 mm	CHW-GX6	550 A	35 V	AC	70 Hz
3	Φ 3.2 mm	CHW-GX6	450 A	40 V	AC	70 Hz
Current Phase Difference	90 deg					
Pipe Size	Φ 762 x 15.9 mm					
Steel Grade	X70					
Flux	CHF-101GX					
Welding Speed	1.3 m/min					

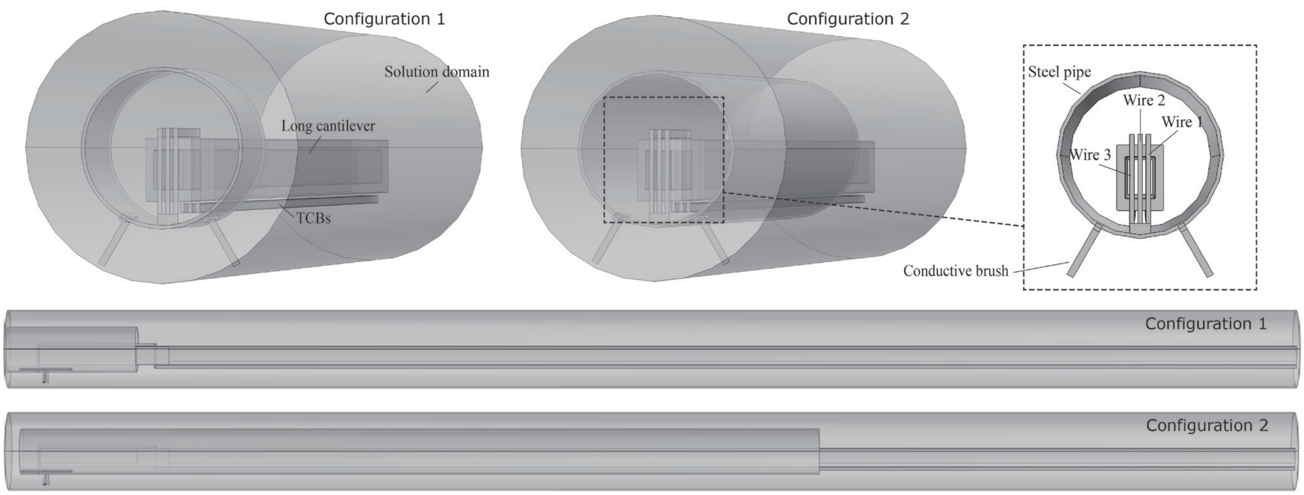

Fig. 4 — COMSOL Multiphysics 3D models for configurations one and two.

Table 2 — Configuration Details and Coordinates of the Magnetic Measurement Points

Configuration	TCB Fixation Location	The Center-to-Center Distance between the TCB and LCWT	Distance between Tube End and Cantilever Fixed End
1	Beneath the cantilever	177 mm	19 m
2	Beneath the cantilever	177 mm	7.4 m
3	Above the cantilever	165 mm	19 m
4	Above the cantilever	165 mm	7.4 m
Measurement Point		Coordinates	
	x/mm	y/mm	z/m
1	0	-200	14
2	0	-200	12
3	0	-200	10
4	0	-200	8
5	0	-200	6
6	0	-215	12
7	0	-225	12
8	0	210	12
9	0	310	12
10	0	400	12

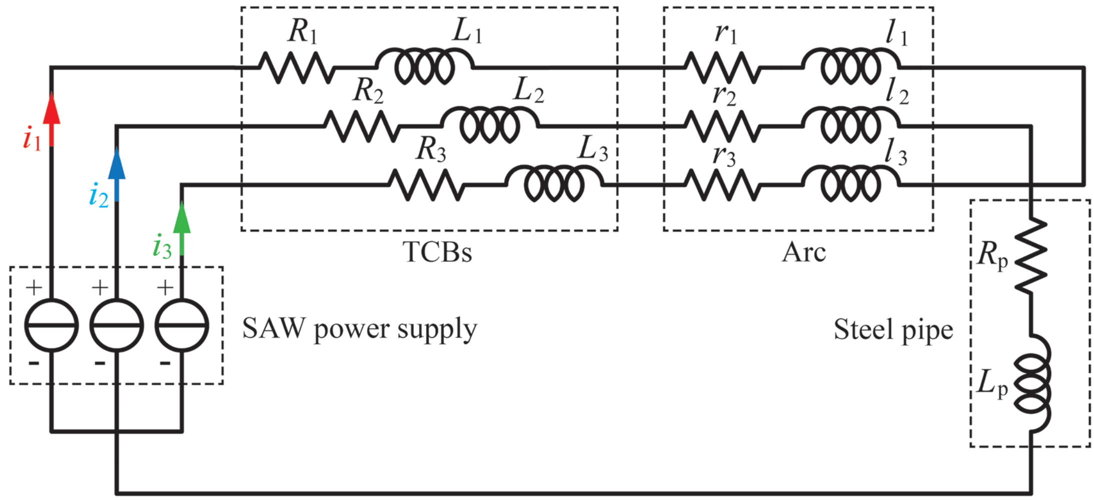

Fig. 5 — Schematic diagram of welding circuit.

roll tracks, ensuring the helix angle corresponded to the spiral joint angle. The experimental parameters were consistent with those of the standard pipe production process, as detailed in Table 1. For practicality and cost-effectiveness, only a portion of the pipe was welded in each welding operation. The cantilever was initially constrained and released only after the welding process had stabilized to minimize the potential distortion of measurement results due to cantilever vibrations.

To investigate the correlation between the vibration of the LCWT and the positioning of the pipe and TCBs, a series of experiments were conducted with various TCB placements and steel pipe locations. For clarity, a Cartesian coordinate system was established, with the origin at the center of the cantilever's fixed end (see Fig. 2A). Four welding configurations were defined, as shown in Fig. 3, and the details of the configurations are listed in Table 2. Note that the standard welding configurations in steel pipe production correspond to configurations 2 and 4, whereas configurations 1 and 3 were employed exclusively for experimental comparison.

Ten magnetic flux density measurement points were selected in space, as illustrated in Fig. 3C, with coordinates listed in Table 2. The measurements at points 1–5 were used to investigate the axial magnetic field distribution, while points 2 and 6–10 were used to investigate the circumferential distribution. To obtain a three-dimensional vector of the magnetic flux density at each point, the one-dimensional gaussmeter was reoriented multiple times to measure the three orthogonal components at the same point under identical conditions.

Finite Element Simulation Setup

The magnetic field of steel pipes during MSAW was simulated using COMSOL Multiphysics, an FE analysis software, and the magnetic loads on the LCWT were calculated. This software allows for the creation of intricate numerical models that incorporate various physical fields and governing equations through a graphical interface. This study utilized the Magnetic Fields and Circuit module in COMSOL Multiphysics 6.1 to develop the simulation models. The computations were done on a server powered by two Intel Xeon Gold 6226R CPUs (2.9 GHz) with 256 GB of DDR4 memory.

Four FE model cases were established to correspond with the four configurations. Figure 4 depicts the FE models for configurations 1 and 2. Each model comprised an LCWT, a steel pipe, three TCBs with welding wires, and conductive brushes, which were all scaled to match the actual dimensions with necessary simplifications. LCWT, with a high aspect ratio, was modeled as a uniform beam. Components on the LCWT, such as the wire feeding mechanism and the electromechanical components, were excluded, and only the shell was considered. The distinction between FE model cases for configurations 3 and 4, compared to configurations 1 and 2, was the TCB positioning above the LCWT. In all cases, a cylindrical electromagnetic field-solving domain was defined. A larger domain enhances accuracy at the expense of computational expense. Consequently, the radius of the cylindrical domain was set to twice that of the steel pipe to balance these factors. The simulation focused on magnetic effects, omitting detailed modeling of welding phenomena such as plasma jets and thermal effects at the weld location. These phenomena were negligible in scale compared to the overall model and had minimal impact on the magnetic field simulation results within the solution domain. The properties of the above model are presented in Table 3.

The circuit module in COMSOL Multiphysics was employed to power the TCBs and welding wires. Figure 5 shows the schematic of the welding circuit. In this setup, the circuit loads comprised three TCBs with welding wires, arcs, and steel pipe, which are modeled as a cascade of resistance and inductance. The SAW power supplies were idealized as current sources, with the first source delivering DC and the subsequent two sources generating square-wave AC. The expression for output current over time is as follows:

$$i_1(t) = A_1\varepsilon(t) \tag{1}$$

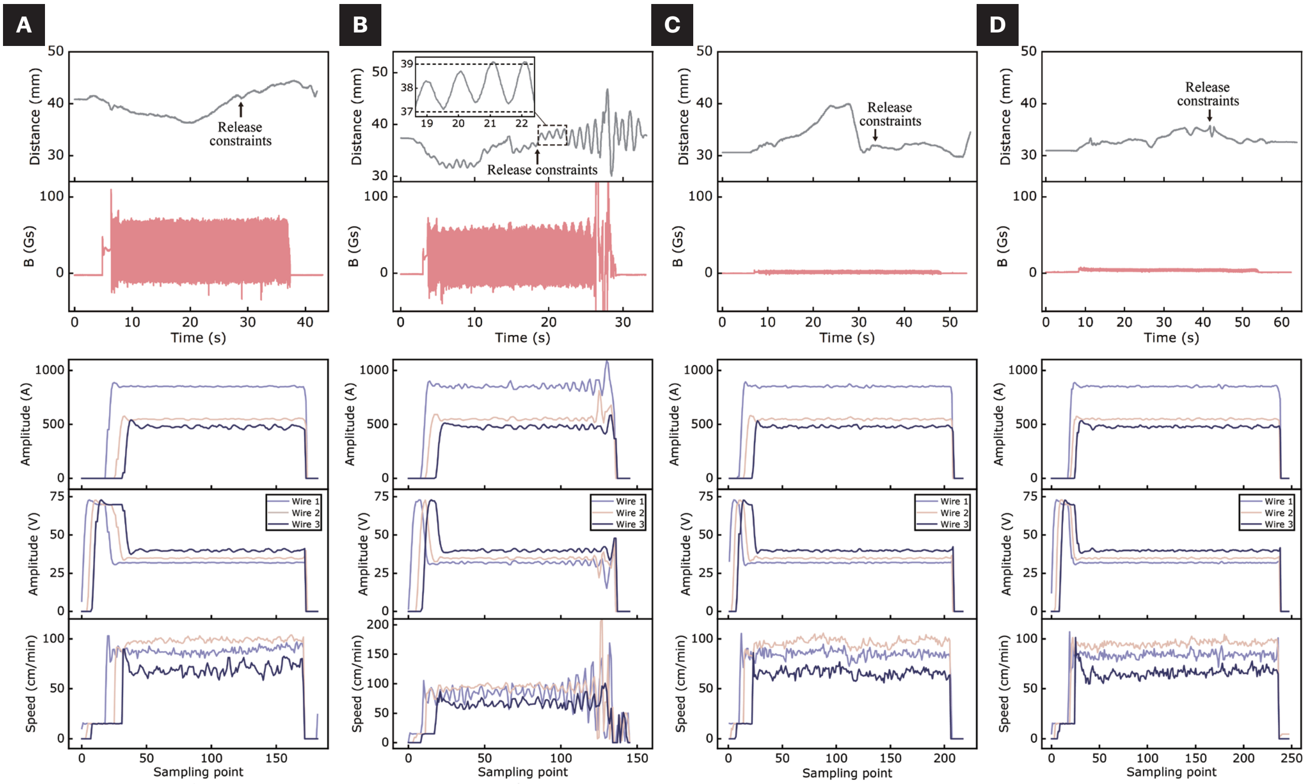

Fig. 6 — Experimental results under various configurations: A–D — Present the results for configurations one to four, respectively.

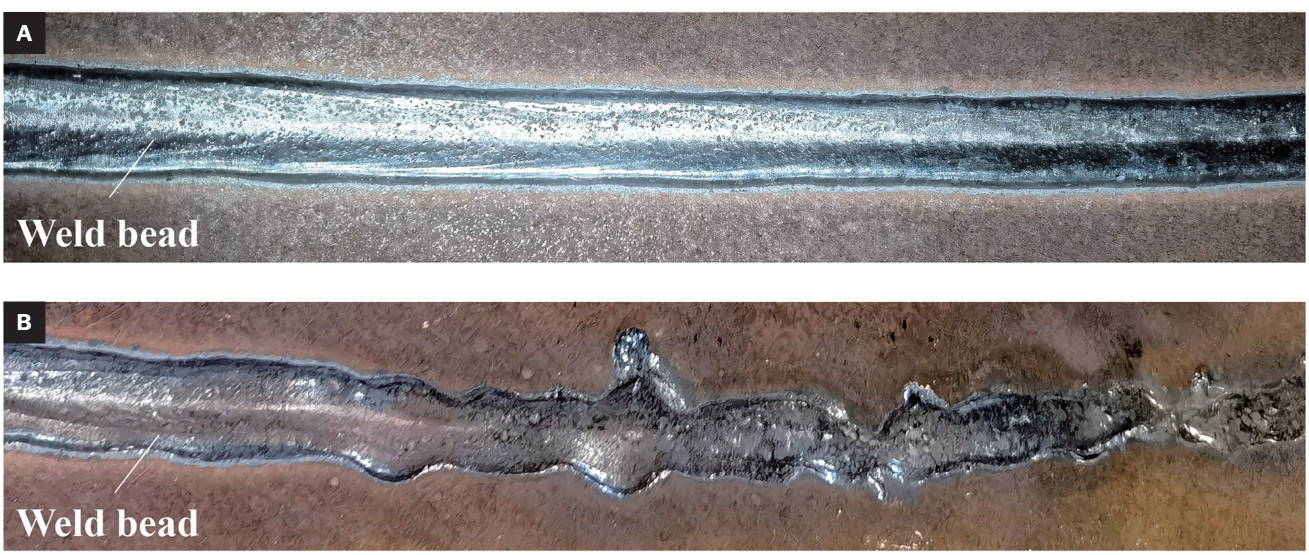

Fig. 7 — Typical weld beam images: A — Normal weld bead; B — weld bead with poor consistency.

$$i_2(t) = A_2 square(2\pi f t)\varepsilon(t) \quad (2)$$

$$i_3(t) = A_3 square(2\pi f t - \frac{\pi}{2})\varepsilon(t) \quad (3)$$

where A_1, A_2, and A_3 denote the current amplitudes, which werw set at 850 A, 550 A, and 450 A, respectively; f denote the welding current frequency, which was set at 70 Hz; $\varepsilon(t)$ denotes the step function, defined such that $\varepsilon(t) = 0$ for $t <$ 0 and $\varepsilon(t) = 1$ otherwise. To enhance convergence, the step function was smoothed with a transition zone of 0.1 s.

Table 3 — The Properties of the Model Components

Components	Material	Relative Permittivity (ε_r)	Relative Permeability (μ_r)	Electrical Conductivity (σ)[S/m]
Cantilever	Iron	1	200	1.12×10^7
TCB	Copper	1	1	5.998×10^7
Steel Pipe	Iron	1	200	1.12×10^7
Brush	Copper	1	1	5.998×10^7
Others	Air	1	1	0

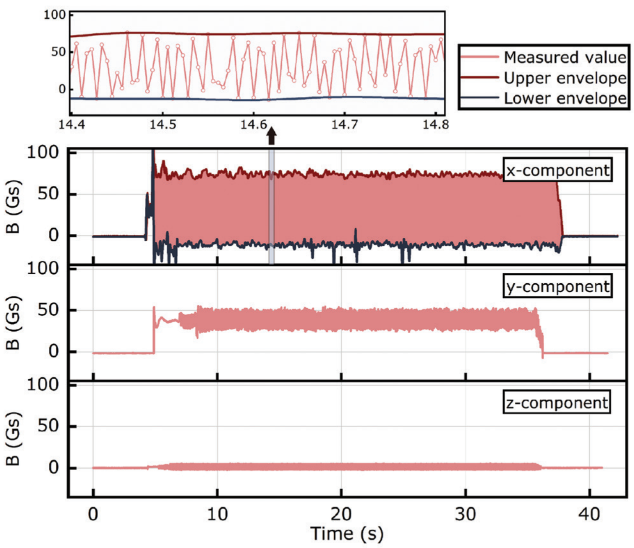

Fig. 8 — The x, y, and z components of magnetic flux density at point two for configuration one.

The magnetic field distribution in the solution domain satisfied Maxwell's equation:

$$\nabla \cdot \boldsymbol{D} = \rho_e \tag{4}$$

$$\nabla \cdot \boldsymbol{B} = 0 \tag{5}$$

$$\nabla \times \boldsymbol{E} = -\frac{\partial \boldsymbol{B}}{\partial t} \tag{6}$$

$$\nabla \times \boldsymbol{H} = \boldsymbol{J} + \frac{\partial \boldsymbol{D}}{\partial t} \tag{7}$$

$$\boldsymbol{B} = \nabla \times \boldsymbol{A} \tag{8}$$

where $\boldsymbol{D}$ is the electric flux density, $\boldsymbol{E}$ is the electric field intensity, $\boldsymbol{J}$ is current density, $\boldsymbol{A}$ is magnetic potential, $\boldsymbol{B}$ is magnetic flux density, and $\boldsymbol{H}$ is magnetic field intensity.

The following equations govern the constitutive relations for electromagnetic field quantities:

$$\boldsymbol{B} = \mu_0 \mu_r \boldsymbol{H} \tag{9}$$

$$\boldsymbol{D} = \varepsilon_0 \varepsilon_r \boldsymbol{E} \tag{10}$$

$$\boldsymbol{J} = \sigma \boldsymbol{E} \tag{11}$$

where μ_0 is the vacuum permeability, μ_r is the relative permeability of the medium, ε_0 is the vacuum permittivity, ε_r is the relative permittivity, and σ denotes the material's electrical conductivity

The magnetic insulation boundary condition was applied to the solving space:

$$\boldsymbol{n_d} \times \boldsymbol{A} = 0 \tag{12}$$

where $\boldsymbol{n_d}$ denotes the normal vector to the surface of the solution domain.

The initial conditions were as follows:

$$\boldsymbol{A} = \boldsymbol{0} \tag{13}$$

The Maxwell stress tensor $\boldsymbol{T}$ was introduced as follows:

$$T_{ij} = \varepsilon_0 \left(E_i E_j - \frac{1}{2} \delta_{ij} E^2 \right) + \frac{1}{\mu_0} (B_i B_j - \frac{1}{2} \delta_{ij} B^2) \tag{14}$$

where δ_{ij} denotes the Kronecker delta, which defined $\delta_{ij} = 1$ when $i = j$ and$\delta_{ij} = 0$ otherwise.

The electromagnetic force per unit surface area of an object in a low-frequency electromagnetic field can be calculated using the following formula:

$$\frac{d\boldsymbol{F}_A}{\mathrm{d}a} = \boldsymbol{T}\cdot\boldsymbol{n} \tag{15}$$

where $\boldsymbol{n}$ donates the normal vector of the surface element and a donates the surface area.

The expression for the load distribution f(z,t) on the cross-section of long cantilever at the coordinate z is as follows:

$$f(z,t) = \lim_{\Delta z\to 0}\frac{\oiint T\cdot n\,\mathrm{d}s}{\Delta z} = \lim_{\Delta z\to 0}\frac{\iint T\cdot n\,\mathrm{d}z\mathrm{d}c}{\Delta z} = \oint T\cdot n\,\mathrm{d}c \tag{16}$$

where c donates the curve of the cross-sectional shape.

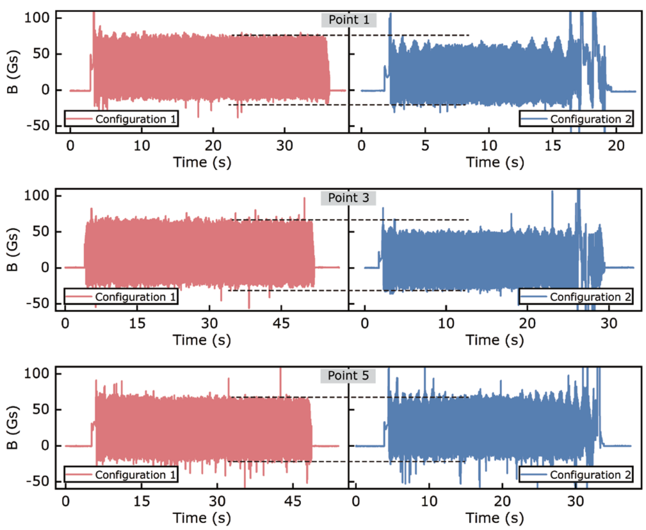

Fig. 9 — The x-component of magnetic flux density of points 1–5 for configurations one and two.

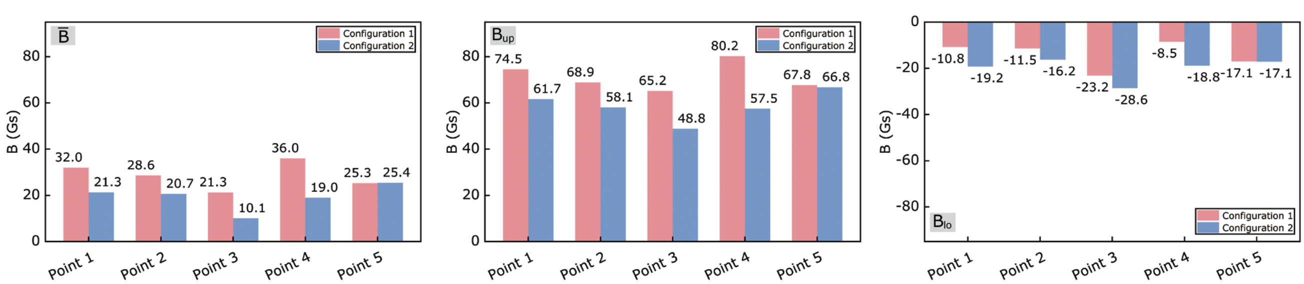

Fig. 10 — The magnetic field indices of magnetic flux density of points 1–5 for configurations one and two.

Table 4 — The Properties of the Beam Model

Property	Symbol	Value
Modulus of Elasticity	E	200 GPa
Media Density	ρ	7850 kg/m^3
Cross-Section Area	A_C	0.0326 m^2
Length	L	20 m
The Area Moment of Inertia	I	3.0269×10^{-4} m^4

Analytical Model of LCWT Vibration

The vibration of the LCWT affects the arc length, which modifies the arc's load characteristics. These changes impact the output voltage and current of welding power supplies and subsequently influence the magnetic field. Additionally, vibration induces adjustments in the wire feed speed within the arc voltage feedback system. This study does not delve into a detailed examination of the dynamic system characteristics in pipe MSAW. Instead, a simplified analytical model for LCWT vibration was established based on the following assumptions and premises:

1. The influence of arc length variations on the arc's load characteristics is neglected, and the amplitude of output voltage and current are assumed to be constant.

2. The LCWT is approximated as a beam with a large aspect ratio and uniform cross-section.

3. The beam deformation is minor and elastic, and the effects of medium dissipation are neglected.

Under assumptions two and three, the LCWT can be modeled using the Euler-Bernoulli beam theory, as detailed in textbooks and literature (Ref. 21). The equation governing its transverse vibration is as follows:

$$\rho A_c \frac{\partial^2 v(z,t)}{\partial t^2} + EI\frac{\partial^4 v(z,t)}{\partial z^4} = f_{tr}(z,t) \tag{17}$$

where the meaning and numerical values of the symbols are given in Table 4. $v(z,t)$ is the transverse deflection at the axial location z and time t; $f_{tr}(z,t)$ is the transverse force per unit length, which is the x-y plane component of $f(z, t)$. The effects of axial loads on LCWT were neglected in this model, and the validity of this approach is discussed in the "Results" section.

The beam was fixed at one end and free at the other, with the following boundary conditions:

$$v(z,t)|_{z=0} = 0;\ \frac{\partial v(z,t)}{\partial z}|_{z=0} = 0;\ \frac{\partial^2 v(z,t)}{\partial z^2}|_{z=L} = 0;\ \frac{\partial^3 v(L,t)}{\partial z^3}|_{z=L} = 0 \tag{18}$$

$$v(z,t)|_{t=0} = 0;\ v(\dot{z},t)|_{t=0} = 0 \tag{19}$$

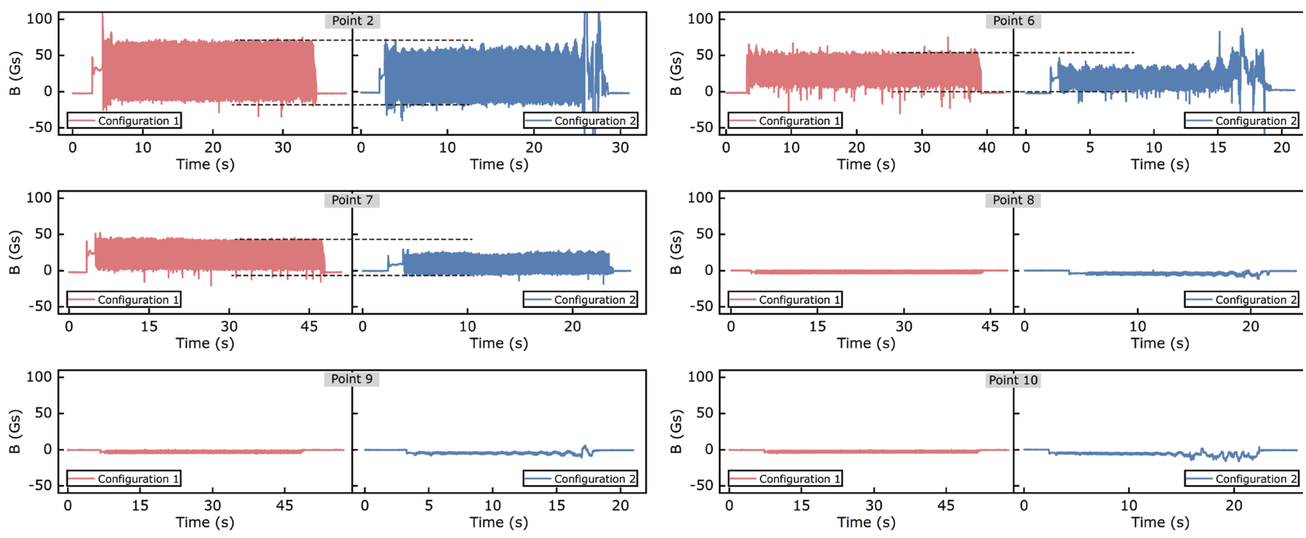

Fig. 11 — The x-component of magnetic flux density of points 2, 6–10 for configurations one and two.

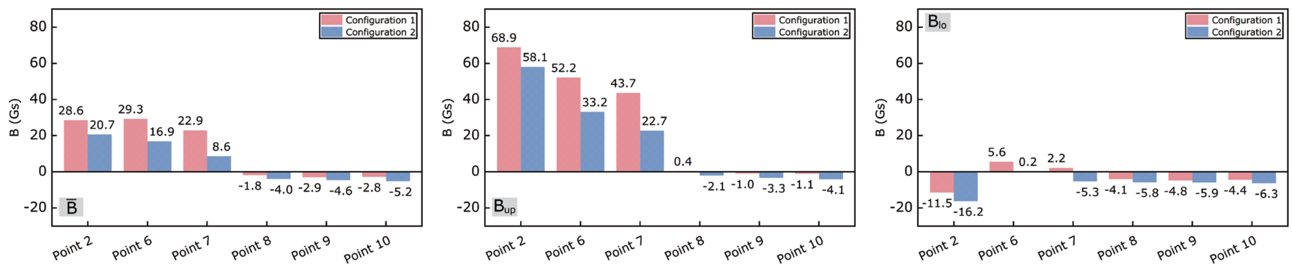

Fig. 12 — The magnetic field indices of magnetic flux density of points 2, 6–10 for configurations one and two.

Results

Measurement Results Under Various Configurations

Figure 6 presents experimental data for displacement, magnetic flux density, and power supply output for four welding configurations. The welding process was stable for configurations 1, 3, and 4, as evidenced by the consistent amplitude in the magnetic field-time curves and the relatively constant output of the power supply. Additionally, the displacement measured at the torch end exhibited a slow variation within a small range. Configuration 2 exhibited unstable welding behavior. The LCWT remained stable at the outset due to applied constraints, but instability and low-frequency vibrations occurred when constraints were removed. The initial vibration amplitude was 1–2 mm, which subsequently increased. Concurrently, the output of the welding power supply and the wire feed speed became unstable and exhibited oscillatory behavior, accompanied by fluctuations in the amplitude of the magnetic induction. The stable welding processes yielded weld beads with good consistency (Fig. 7A), while the unstable process resulted in beads with poor quality (Fig. 7B).

Magnetic Field Distribution

To illustrate the magnetic field, the x, y, and z components of the magnetic flux density at point 2 of configuration 1 are depicted in Fig. 8 as examples. The magnetic field frequency was 70 Hz, which matched the welding current. Of the three components, the x-component was dominant, while the z-component was negligible. Consequently, the analysis of the magnetic field was based on the x-component. The magnetic field-time curve was divided into intervals, each with a fixed number of sampling points. Spline interpolation was then applied to the maxima and minima of these intervals to construct upper and lower envelopes. The magnetic field indices (MFI) $\bar{B}$, $\bar{B}_{up}$, and $\bar{B}_{lo}$ were defined as follows:

$$\bar{B} = \frac{1}{|N_{sp}|}\sum_{n=N_{st}+1}^{N_{st}+N_{sp}} B(n) \tag{20}$$

$$\overline{B_{up}} = \frac{1}{|N_{sp}|}\sum_{n=N_{st}+1}^{N_{st}+N_{sp}} B_{up}(n) \tag{21}$$

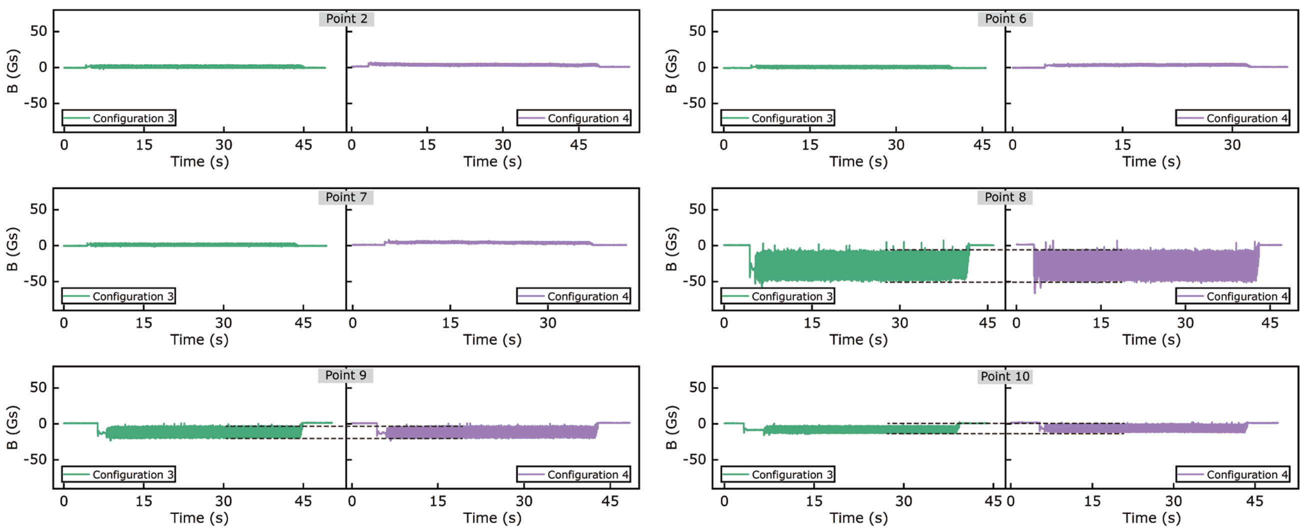

Fig. 13 — The x-component of magnetic flux density of points 2, 6–10 for configurations three and four.

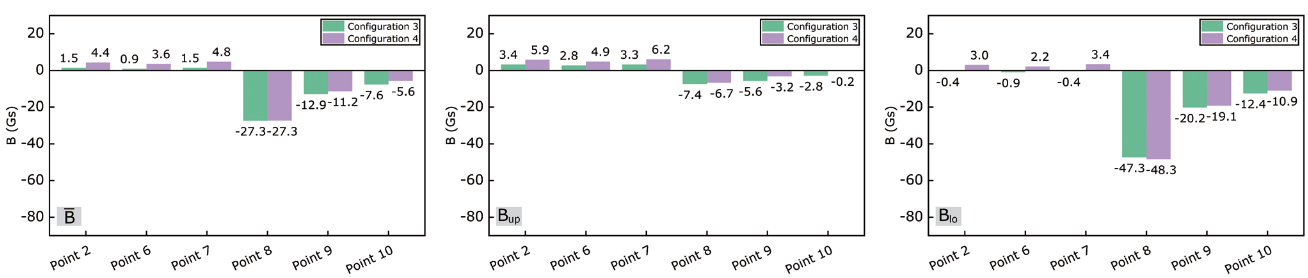

Fig. 14 — The magnetic field indices of magnetic flux density of points 2, 6–10 for configurations three and four.

$$\overline{B_{lo}} = \frac{1}{|N_{sp}|}\sum_{n=N_{st}+1}^{N_{st}+N_{sp}} B_{lo}(n) \tag{22}$$

where $B(n)$ as the measured value of the magnetic flux density, $B_{up}(n)$ and $B_{lo}(n)$ were the upper and lower envelopes, respectively; and N_{st} and N_{sp} donated the starting sampling point and the sampling number, respectively. N_{st} corresponded to the sample point 5 s after welding started, and N_{sp} was set to 1000, during which the LCWT was constrained and the amplitude of magnetic flux density remained essentially consistent.

Figure 9 displays the magnetic flux density measurements at points 1 to 5 for configurations 1 and 2, while Fig. 10 shows the corresponding MFI for these locations. As shown in Fig. 9, the magnetic field-time curves at points 1–4 in configuration two, which were inside the pipe, shifted downward compared to those in configuration 1. This shift was also reflected in the decrease in MFI for points 1 to 4, as evidenced in Fig. 10. Measurement point 5, which was located outside the pipe

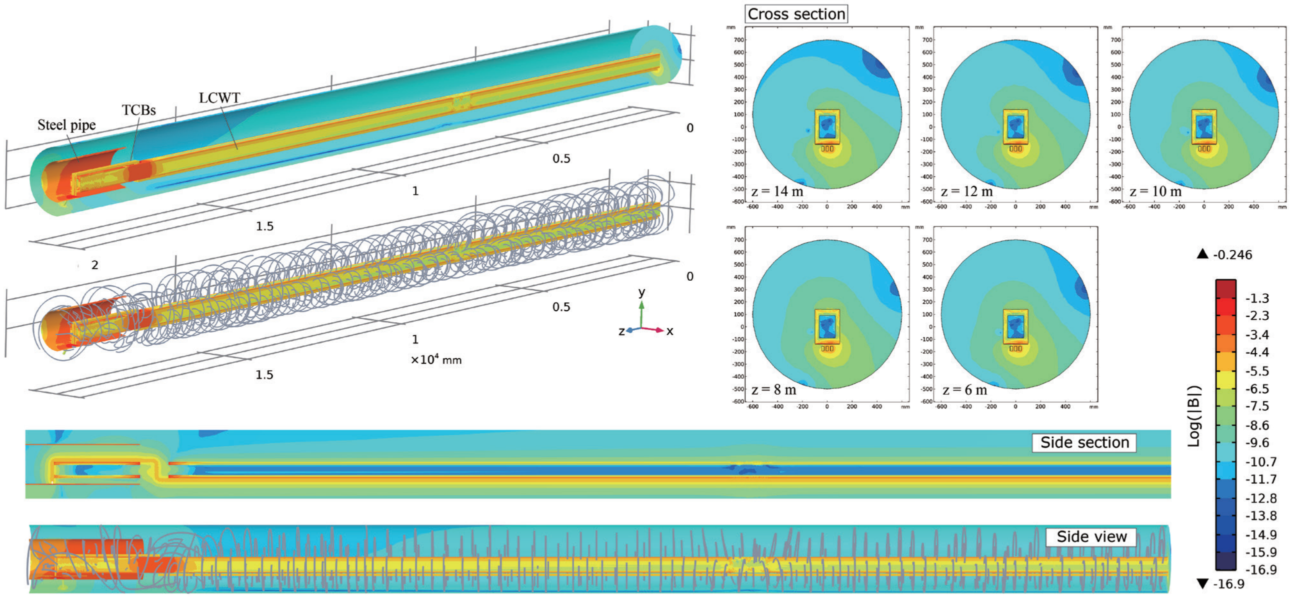

Fig. 15 — The simulation results of magnetic flux density distribution and magnetic flux lines for configuration one.

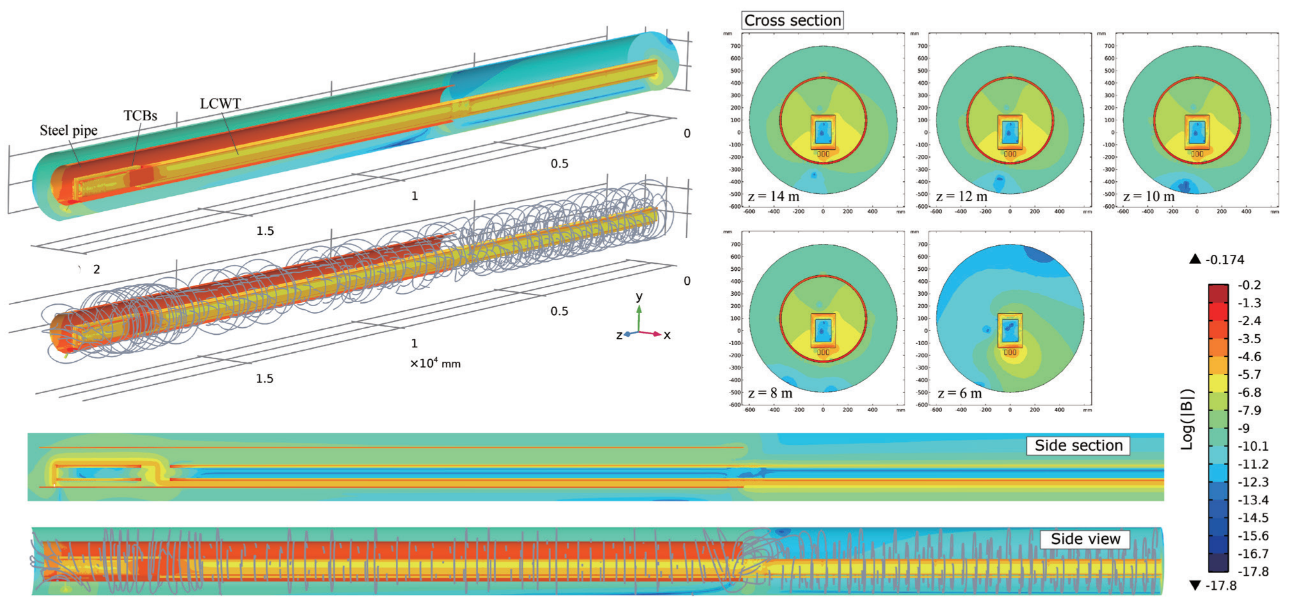

Fig. 16 — The simulation results of magnetic flux density distribution and magnetic flux lines for configuration two.

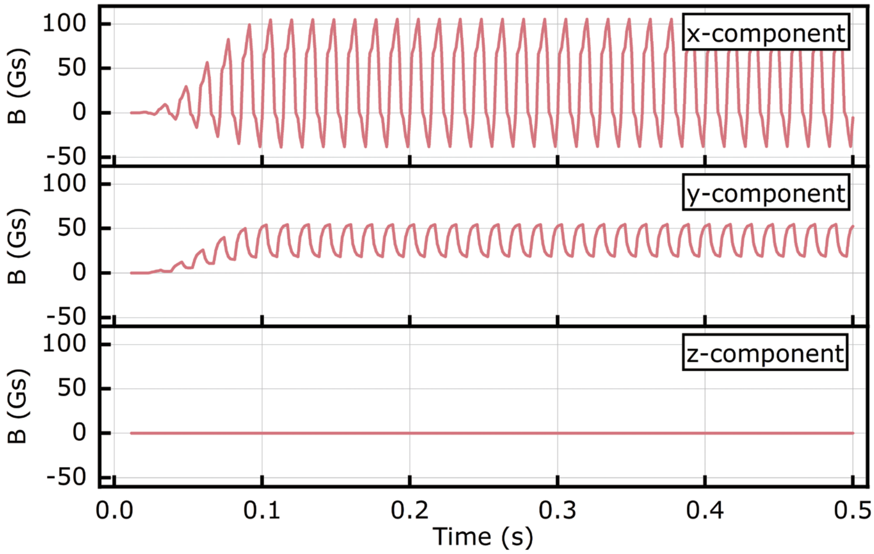

Fig. 17 — The x, y, and z components of simulated magnetic flux density of point 2 for configuration one.

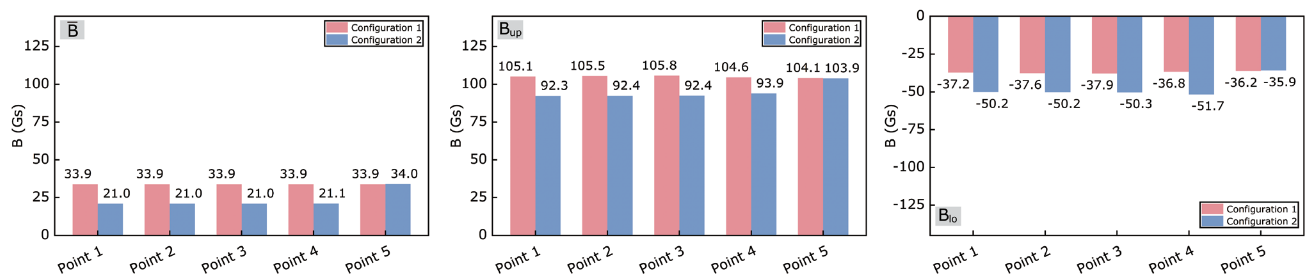

Fig. 18 — The simulated magnetic field indices of magnetic flux density of points 1–5 for configurations one and two.

for both configurations, exhibited consistent magnetic field measurements. Note that the MFIs at points 1–5 for configuration 1 were approximately uniform. Similarly, the MFIs at points 1 to 4 exhibited consistency for configuration 2.

Figure 11 displays the magnetic flux density measurements at points 2, 6 to 10 for configurations 1 and 2, while Fig. 12 shows the corresponding MFIs. Points 2, 6, and 7, which were closer to the TCBs, exhibited prominent magnetic flux density. Conversely, points 8, 9, and 10, located more distant from the TCBs, exhibited negligible magnetic fields. Similar to points 1-4, the magnetic flux density at points 6 and 7 were shifted downward in configuration 2 compared to those in configuration 1. Notably, the reduction was greatest at point 7, closest to the pipe wall, followed by point 6, then the smallest reduction was at point 2, which was farther from the pipe wall.

Figure 13 shows the magnetic flux density measurements at points 2, 6 to 10 for configurations 3 and 4, with Fig. 14 providing the corresponding MFIs. In configurations 3 and 4, with the TCBs located above the LCWT, points 8 to 10 were in closer proximity to the TCBs, and the magnetic flux densities were more significant. In contrast, points 2, 6, and 7 were situated below the TCBs, and the magnetic flux densities were minor. The magnetic flux density at points 2, 6 to 10 in configuration 4 exhibited negligible deviations from that in configuration 3, contrasting with the pronounced differences observed between configurations 1 and 2.

The FE simulations yielded the magnetic field distribution, with the simulation results of configurations 1 and 2 illustrated in Fig. 15 and 16, respectively. Note that the magnetic flux density magnitude was logarithmically scaled for better visualization. Figure 15 shows that the magnetic field in configuration 1 exhibited good axial consistency. For configuration 2 (Fig. 16), the magnetic field within the pipe was approximately consistently distributed axially, except in regions proximate to the pipe ends. The simulations indicated significant magnetic fields near the TCBs, and the magnetic field inside the steel pipe wall was substantially greater than that in other areas of the space due to pipe magnetization. For comparison with experiment data, the magnetic flux density at point 2 on the FE model was calculated, as shown in Fig. 17. Following the transition phase of the first 0.1 s, the magnetic field at point 2 exhibited periodic flux density with a frequency of 70 Hz, matching the frequency of the welding current. Despite higher amplitudes, the simulated magnetic flux density components were generally consistent with those measured in the experiment (Fig. 8).

The model's MFI at points 1 to 10 were calculated for configurations 1 and 2. As shown in Fig. 18, in configuration 1,

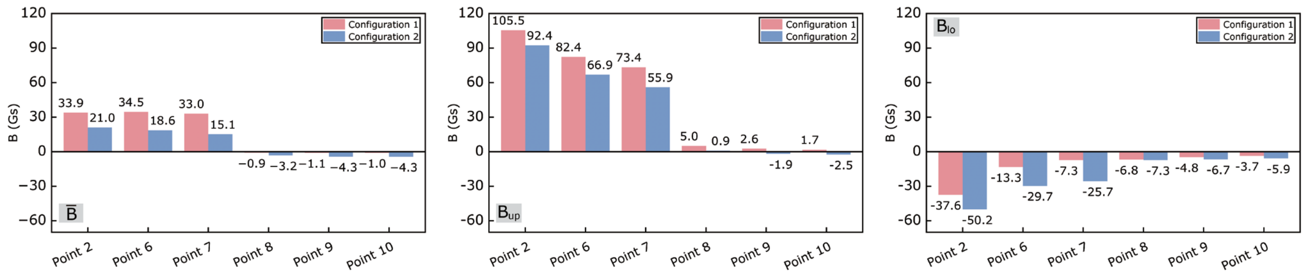

Fig. 19 — The simulated magnetic field indices of magnetic flux density of points 2, 6–10 for configurations one and two.

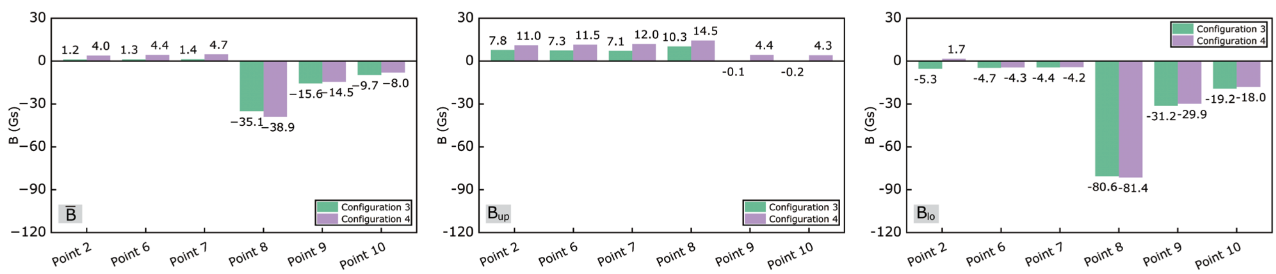

Fig. 20 — The simulated magnetic field indices of magnetic flux density of points 2, 6–10 for configurations three and four.

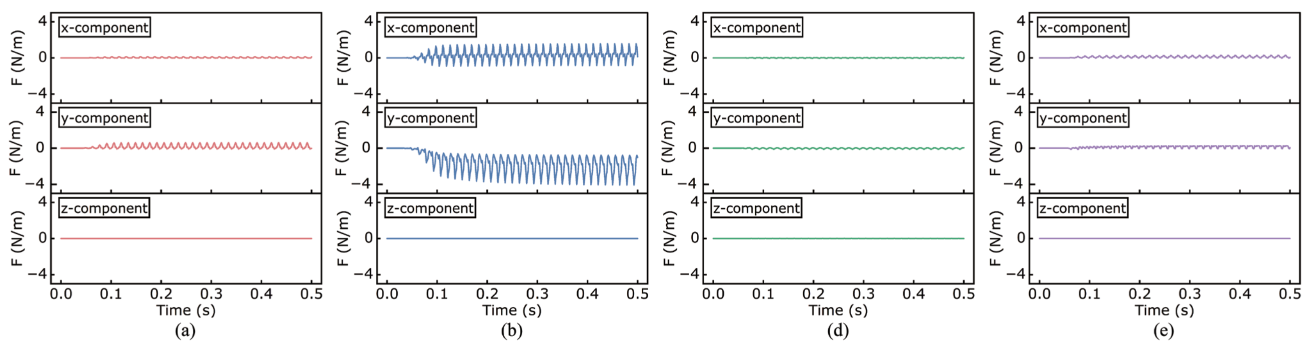

Fig. 21 — The electromagnetic load per unit length on LCWT at coordinate z = 12 m.

the MFIs at points 1 to 5 were essentially identical. In configuration 2, points 1 to 4 were positioned inside the pipe, and the MFIs of these points showed reduced values compared to those in configuration 1. The reductions of these points were observed to be consistent. The MFIs at point 5 showed negligible changes, for point 5 was situated outside the pipe in both configurations 1 and 2. The simulation results for the MFI at points 6 to 10 also revealed a decrease compared to configuration 1, with the magnitude of the reduction varying, as depicted in Fig. 19. Among points 2, 6, and 7, point 2, which was closest to the pipe wall, exhibited a higher reduction in MFI.

Figure 20 illustrates the calculated MFI values at points 2, 6 to 10 for configurations 3 and 4. With the TCBs positioned above the LCWT, the MFIs at points 8, 9, and 10 were significantly higher than those at points 2, 6, and 7. Furthermore, there were minor differences in the MFIs calculated in points 2, 6 to 10 in configurations 3 and 4 in contrast to the pronounced differences observed between configurations 2 and 1.

Electromagnetic Load

Electromagnetic loads on LCWT were calculated based on the results of electromagnetic field simulation. Given the axial consistency of the magnetic field distribution, the position at $z = 12$ m along the LCWT was chosen for load analysis. This location was positioned inside the pipe for configurations one and three, and outside the pipe for configurations two and four. The calculated electromagnetic loads at this position are presented in Fig. 21. Among the four welding configurations, significant electromagnetic loads are observed solely in configuration two. The loads associated with the remaining three configurations were negligible and, thus, are not considered

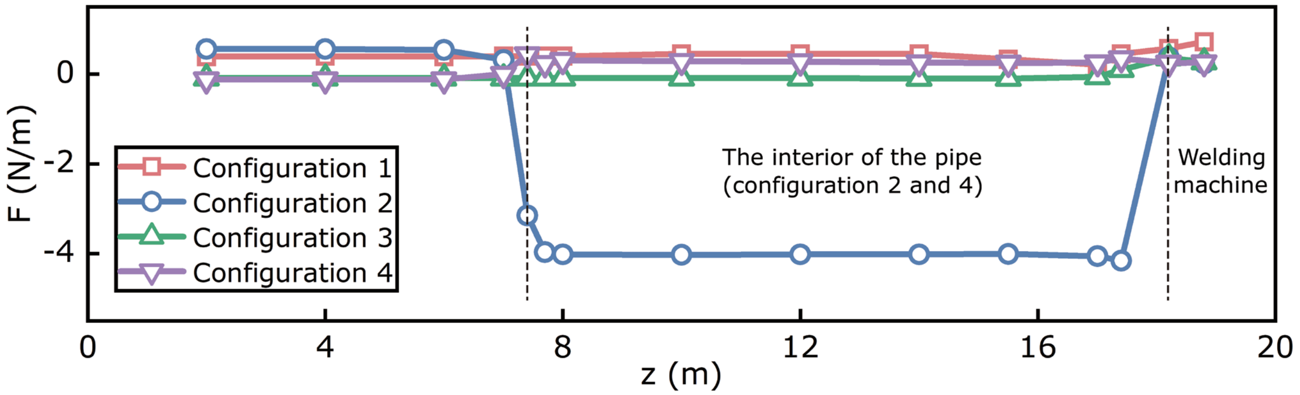

Fig. 22 — The simulated load distribution on LCWT.

further. Notably, the load in configuration two is transverse, primarily oriented along the y-axis, and exhibits periodicity that correlates with the welding current frequency of 70 Hz.

The axial load distribution along the LCWT was additionally computed, as depicted in Fig. 22. Significant electromagnetic load distribution is observed only on the LCWT in configuration two, with negligible loads in other configurations. Regarding configuration two, note that the load distribution on the LCWT is directly related to the pipe's position. Specifically, the load is exclusively imposed on the segment of the LCWT that is positioned inside the pipe, whereas the outer segment remains largely devoid of significant loading. Furthermore, it is notable that the load on the LCWT within the pipe is distributed with approximate uniformity.

The Response of the Long Cantilever Welding Torch

The vibration response analysis of the beam can be confined to configuration two, as the electromagnetic excitation on LCWT is negligible in other configurations. According to the simulation, the analytical expression for the loads on LCWT can be represented by the following equations:

$$f_{tr}(z,t) = F_t(t)P(z)\varepsilon(t) \tag{23}$$

$$P(z) = \begin{cases} 0 & (else) \\ 1 & (z \in (7.4, 18.5)) \end{cases} \tag{24}$$

where $F_t(t)$ denotes a periodic function with a frequency of 70 Hz, characterizing the load fluctuation over time, $P(z)$ serves as an indicator function delineating the spatial distribution of the load across LCWT; and interval (7.4,18.5) represents the portion of the long cantilever located within the pipe.

The response of LCWT under electromagnetic loads is calculated via modal superposition, with the derivation in Appendix I. An approximate solution of the displacement-time equation for the LCWT's end is provided as follows:

$$v_L(t) = -0.5322\big(1 - \cos(4.275t)\big)[mm] \tag{25}$$

Upon releasing the constraints, the cantilever's end exhibits a maximum deflection of 1.06 mm from its initial position, in concordance with our experimental measurements.

Discussion

Both experimental and simulation results confirm the magnetization of steel pipes in the welding process. More importantly, magnetized steel pipes are found to induce magnetic fields and influence the magnetic field distribution within the pipe. As illustrated in Figs. 10 and 18, the MFI variations at points 1–4 for configuration two, as compared to configuration one, result from the altered positions of these points relative to the pipe. In configuration one, points 1–4 are situated outside the pipe and at a significant distance, whereas in configuration two, they are positioned inside the pipe. With the welding parameters constant, the magnetic field contributions induced by the welding circuit current are roughly equivalent for both configurations. Consequently, the observed MFI variations confirm and characterize the influence of the "additional" magnetic field generated by the magnetized steel pipe. In Fig. 9, the measurement results at point 4 for configuration two further demonstrate the impact of the magnetic field from the steel pipe. As welding progresses, the location of point 4 shifts from the interior to the exterior of the pipe, and a transition phase of the measured magnetic field can be observed, which demonstrates the diminishing and eventual disappearance of the steel pipe's magnetic field influence.

In the studied case, the magnetic field induced by the magnetized steel pipe is approximately uniform along the steel pipe's axial direction, as shown in Fig. 16. This uniformity can be attributed to the cantilever and steel pipe's large aspect ratios and their approximately consistent cross-sectional areas along the z-axis, suggesting a form of translational symmetry, which is also corroborated by experimental results, as shown in Fig. 10. Despite the deviations from the idealized finite element model in real welding equipment, and considering instrumental precision and measurement errors, the measured magnetic field consistency at points 1–4 is slightly less than the simulation results (see Fig. 18). However, it is still within an acceptable error range, suggesting that the axial uniformity is valid.

The magnetic field excited by the pipe is related to the location of the TCBs, which acts as the magnetizing field source. As shown in Figs. 14 and 20, with the TCBs positioned above the LCWT, the magnetic field at the measurement points 2, 6–10 shows no significant difference under inside-pipe versus outside-pipe conditions, suggesting that the magnetic field excited by the magnetized steel pipe is negligible. In comparison, when TCBs are secured below the LCWT, significant variations are observed at these points under inside-pipe versus outside-pipe conditions (see Figs. 12 and 19), indicating a more significant magnetic field contribution from the magnetized pipe.

The magnetic field of the magnetized steel pipe is considered the causal factor for the LCWT vibration. As shown in Fig. 6, although LCWT is predominantly positioned within the pipe in configurations two and four, vibration is only observed in configuration two, where the magnetized steel pipe generates a significant magnetic field within the pipe's interior. In contrast, no obvious cantilever vibration was observed in configuration four, as the influence of the steel pipe's magnetic field is relatively minor. Simulation and analytical results further reveal the mechanism by which the steel pipe's magnetic field causes LCWT vibration. As shown in Figs. 21 and 22, the magnetized steel pipe applies high-frequency (70 Hz) electromagnetic loads through the magnetic field to the LCWT within the pipe, resulting in small amplitude, low-frequency vibrations.

The experimental and simulation findings can inform the design and optimization of inner-diameter welding equipment. Designers must consider the magnetizing effects of welding circuit currents and potential magnetic interactions with the magnetized steel pipe, particularly for equipment with lower rigidity structures such as cantilever beams. Optimizing the placement of welding cables is essential to mitigate magnetic interactions and maintain stability in welding, as the cable currents influence pipe magnetization, leading to magnetic forces acting on the equipment from the pipe.

Conclusion

This study employs a combination of experiments and finite element simulations to model the magnetic field in oil and gas pipes inside MSAW. It identifies the physical mechanisms of the vibration of the LCWT used in welding, providing a foundation for spiral pipe final-welding system optimization. The study's conclusions are as follows:

1. In the scenario of steel pipe MSAW, the magnetic field excited by the welding current is a significant issue, as it magnetizes the steel pipe, which in turn interacts with other welding equipment through its magnetic field and affects the stability of the welding process.

2. In the case studied, with the LCWT and pipe having a large length-to-diameter ratio and nearly equal cross-sections, the magnetic field induced by the steel pipe is approximately uniformly distributed along the axial direction. The influence of the steel pipe is dependent on the location of the TCBs, which function as the excitation source. When the TCB is close to the pipe wall, the magnetized steel pipe significantly contributes to the magnetic field within the pipe. Conversely, this contribution becomes negligible when the TCB is farther away.

3. The magnetized steel pipe imposes electromagnetic loads on the long cantilever through the magnetic field it excites, thereby causing vibrations. Optimizing the position of the TCB can diminish the magnetic field contribution from the magnetized steel pipe, reducing LCWT vibration and improving welding process stability.

4. To ensure welding process stability, the design of inner-diameter welding equipment, especially those with low rigidity, must consider the magnetization of the steel pipe and the magnetic forces between the pipe and the equipment.

Acknowledgments

This study was performed under Enterprises and institutions entrusting Tsinghua University with scientific and technological projects (Contract No. 20212001757).

References

1. Mathias, L. L. S., Sarzosa, D. F. B., and Ruggieri, C. 2013. Effects of specimen geometry and loading mode on crack growth resistance curves of a high-strength pipeline girth weld. *International Journal of Pressure Vessels and Piping* 111–112(11): 106–19. DOI: 10.1016/j.ijpvp.2013.06.003

2. Feng, Y., Ji, L., Chen, H., Jiang, J., Wang, X., Ren, Y., Zhang, D., Niu, H., Bai, M., and Li, S. 2021. Research progress and prospect of key technologies for high-strain line pipe steel and pipes. *Natural Gas Industry B* 8(2): 146–53. DOI: 10.1016/j.ngib.2020.09.015

3. Felber, S. 2008. Welding of the high grade pipeline-steel X80 and description of different pipeline-projects. *Welding in the World* 52(5–6): 19–41. DOI: 10.1007/BF03266637

4. Kozuki, S., Hayakawa, N., and Rinsei, I. 2017. Arc behavior in four electrodes submerged-arc welding. Paper presented at the *The 27th International Ocean and Polar Engineering Conference*, San Francisco, Calif. ISOPE-I-17-404.

5. Tušek, J., and Suban, M. 2003. High-productivity multiple-wire submerged-arc welding and cladding with metal-powder addition. *Journal of Materials Processing Technology* 133(1–2): 207–13. DOI: 10.1016/S0924-0136(02)00235-2

6. Kiran, D. V., and Na, S. 2014. Experimental studies on submerged arc welding process. *Journal of Welding and Joining* 32(3): 1–10. DOI: 10.5781/JWJ.2014.32.3.1

7. Sengupta, V., Havrylov, D., and Mendez, P. F. 2019. Physical phenomena in the weld zone of submerged arc welding — A review. *Welding Journal* 98(10): 283-s to 313-s. DOI: 10.29391/2019.98.025

8. Ridings, G. E., Thomson, R. C., and Thewlis, G. 2002. Prediction of Multiwire Submerged Arc Weld Bead Shape Using Neural Network Modelling. *Science and Technology of Welding and Joining* 7(5): 265–79. DOI: 10.1179/136217102225006822

9. Scutelnicu, E., Rusu, C. C., Georgescu, B., Mircea, O., and Bormambet, M. 2017. Mechanical behaviour of welded joints achieved by multi-wire submerged arc welding. *Advanced Materials Research* 1143(2): 52–57. DOI: 10.4028/www.scientific.net/AMR.1143.52

10. Layus, P., Kah, P., Martikainen, J., Gezha, V. V., and Bishokov, R. V. 2014. Multi-wire SAW of 640 MPa Arctic shipbuilding steel plates. *The International Journal of Advanced Manufacturing Technology* 75(5–8): 771–82. DOI: 10.1007/s00170-014-6147-2

11. Zhao, M., Feng, X., Cui, Z., Wang, J., and Chen, H. 2022. Influence of transverse auxiliary magnetic field on weld formation and joint

quality in spiral submerged arc welding of X80 steel linepipe. *Welding in the World* 66(12): 2497–2508. DOI: 10.1007/s40194-022-01371-9

12. Chen, X., Lu, H., Chen, G., and Wang, X. 2015. A comparison between fracture toughness at different locations of longitudinal submerged arc welded and spiral submerged arc welded joints of API X80 pipeline steels. *Engineering Fracture Mechanics* 148(11): 110–21. DOI: 10.1016/j.engfracmech.2015.09.003

13. Knoop, F. M., and Sommer, B. 2004. Manufacturing and use of spiral welded pipes for high pressure service: state of the art. *2004 International Pipeline Conference 1–3*: 1761–69. DOI: 10.1115/IPC2004-0257

14. Knoop, F. M. 2015. "Pipe manufacture—spiral pipe." In *Oil and Gas Pipelines*, edited by Revie, R. W., 195–202. New Jersey: John Wiley & Sons. DOI: 10.1002/9781119019213.ch13

15. Chen, J., Han, Z., Wang, L., and Wu, C. 2020. Influence of arc interactions on heat and mass transfer during a two-arc hybrid welding. *International Journal of Heat and Mass Transfer* 148(2): 119058. DOI: 10.1016/j.ijheatmasstransfer.2019.119058

16. Chen, D., Chen, M., and Wu, C. 2015. Effects of phase difference on the behavior of arc and weld pool in tandem P-GMAW. *Journal of Materials Processing Technology* 225(11): 45–55. DOI: 10.1016/j.jmatprotec.2015.05.022

17. Cho, D-W. 2018. "Modeling and analysis of molten pool behavior for submerged arc welding process with single and multi-wire electrodes." In *Heat and Mass Transfer – Advances in Modelling and Experimental Study for Industrial Applications,* edited by Ren, Y. Rijeka, Croatia: IntechOpen. DOI: 10.5772/intechopen.76725

18. Kiran, D. V., Cho, D. W., Song, W. H., and Na, S. J. 2014. Arc behavior in two wire tandem submerged arc welding. *Journal of Materials Processing Technology* 214(8): 1546–56. DOI: 10.1016/j.jmatprotec.2014.02.023

19. Gou, W., Xia, G., and Feng, Z. 2019. Study on low-frequency magnetic radiation of DC arc welding output cable. *AIP Conference Proceedings*, 020069. DOI: 10.1063/1.5090723

20. Yamaguchi-Sekino, S., Ojima, J., Sekino, M., Hojo, M., Saito, H., and Okuno, T. 2011. Measuring exposed magnetic fields of welders in working time. *Industrial Health* 49(3): 274–79. DOI: 10.2486/indhealth.MS1269

21. Han, S. M., Benaroya, H., and Wei, T. 1999. Dynamics of transversely vibrating beams using four engineering theories. *Journal of Sound and Vibration* 225(5): 935–88. DOI: 10.1006/jsvi.1999.2257

YIFENG ZHOU, **ZHANLI YANG**, **KEMING GUAN**, **BAOHUA CHANG**, and **DONG DU** (*dudong@tsinghua.edu.cn*) are with the Department of Mechanical Engineering, Tsinghua University, Beijing, China. **YANG** is also with Harbin Welding Institute Limited Company, Harbin, , China. **DU** is also with Key Laboratory for Advanced Materials Processing Technology, Ministry of Education, Tsinghua University, Beijing, China.

Appendix

This appendix presents the derivation process of the beam's response, which is solved using the method of separation of variables. First, let $f_{tr}(z,t) = 0$ to obtain the natural frequencies and modals. $v(z,t) = W(z)T(t)$ is separated into two functions such that $v(z,t) = W(z)T(t)$. From equation 17, it follows that:

$$\ddot{T(t)} + \omega^2 T(t) = 0 \tag{A1}$$

$$\frac{d^4 W(z)}{dz^4} - \beta^4 W(z) = 0 \tag{A2}$$

where ω denotes the angular frequency; β is related to ω as follows:

$$\beta^4 = \frac{\rho A_c}{EI}\omega^2 \tag{A3}$$

The boundary condition (18) can be expressed in terms of $W(z)$ as follows:

$$W(z)|_{z=0} = 0; \frac{\partial W(z)}{\partial z}|_{z=0} = 0; \frac{\partial^2 W(z)}{\partial z^2}|_{z=L} = 0; \frac{\partial^3 W(z)}{\partial z^3}|_{z=L} = 0 \tag{A4}$$

Plugging (A3) in (A2), the frequency equation and the modal expression are obtained as follows:

$$\cos\beta L cosh\beta L + 1 = 0 \tag{A5}$$

$$W(z) = C[(cos\beta z - cosh\beta z) - \frac{(cos\beta L + cosh\beta L)}{(sin\beta L + sinh\beta L)}(sin\beta z - sinh\beta z)] \tag{A6}$$

where C is an arbitrary constant. ω for the first five modes are tabulated in Table A1.

The Euler-Bernoulli beam's modes satisfy the orthogonality condition, with specific C_m and C_n such that $W_m(z)$ and $W_n(z)$ are regular modes, yielding:

$$\int_0^L \rho A_c W_m(z) W_n(z) dz = \delta_{mn} \tag{A7}$$

$$\int_0^L EI W_m(z) \frac{d^4 W_n(z)}{dz^4} dz = \omega_n^2 \delta_{mn} \tag{A8}$$

where δ_{mn} is the Kronecker delta symbol. $\delta_{mn} = 1$ when $m = n$; $\delta_{mn} = 0$ otherwise.

The solution $v(z,t)$ of equation 17 can be represented as a summation of modal multiplied by functions $q_r(t)$. Under typical conditions, the energy of beam vibrations is concentrated in the first few modes, and thus it is sufficient to consider only the first five modes for analysis:

$$v(z,t) = \sum_{r=1}^{5} W_r(z) q_r(t) \tag{A9}$$

Plugging (A9) in (17) with the orthogonality condition, and initial condition, the expression of $q_r(t)$ is as follows:

$$q_r(t) = \int_0^t N_r(\tau) \frac{sin\omega_r(t-\tau)}{\omega_r} d\tau \tag{A10}$$

Table A1 — The Characteristic Angular Frequencies for the First Five Modes

r	1	2	3	4	5
ω_r (rad/s)	4.275	26.791	75.024	147.021	243.010

Table A2 — The Characteristic Angular Frequencies for the First Five Modes

r	1	2	3	4	5
K_r	1.0766×10^{-3}	-1.0106×10^{-4}	-2.0206×10^{-5}	1.9704×10^{-6}	-3.1441×10^{-6}

Table A3 — The Value of a_k and φ_k

k	0	1	2	3	4
a_k	-2.1132	1.32926	0.492216	0.172253	0.242708
φ_k	–	0.2008π	-0.8727π	0.7937π	0.1155π

$$N_r(t) = \int_0^L f_{tr}(z,t) W_r(z) dz \tag{A11}$$

Therefore,

$$v(\mathrm{z,t}) = \sum_{r=1}^{5} \frac{W_r(z)}{\omega_r} \int_0^t N_r(\tau) \sin(\omega_r(t-\tau)) d\tau \tag{A12}$$

Plugging (A9) in (17), the expression of the end of LCWT is as follows:

$$v_L(\mathrm{t}) = \sum_{r=1}^{\infty} K_r \int_0^t F_t(\tau) \sin(\omega_r(t-\tau)) d\tau \tag{A13}$$

$$K_r = \frac{W_r(L)}{\omega_r} \int_0^L P(z) W_r(z) dz \tag{A14}$$

The value of K_r can be determined through numerical integration utilizing the available parameters, K_r for the first five modes are tabulated in Table A2. Note that $F_t(\tau)$ is periodic and can be rewritten in the form of a Fourier series. It can be approximately represented by the first four harmonics.

$$F_t(\tau) = a_0 + \sum_{k=1}^{4} a_k \cos(k\omega_o \tau + \varphi_k) \tag{A15}$$

where $\omega_o = 140\pi$, the coefficients a_k and φ_k can be calculated from the simulation results, with values of the first five terms displayed in Table A3. Note that $k\omega_o >> \omega_r (r = 1,2,3,4,5)$, the following equations are satisfied:

$$\begin{aligned} &\int_0^t a_k \cos(k\omega_0 \tau + \varphi_k) \sin(\omega_r(t-\tau)) \, d\tau \\ &= a_k \frac{-\omega_r \cos(\varphi_k)(\cos(k\omega_0 t) - \cos(\omega_r t)) + \sin(\varphi_k)(\omega_r \sin(k\omega_0 t) - k\omega_0 \sin(\omega_r t)))}{k^2 \omega_0^2 - \omega_r^2} \\ &\ll |a_0| \end{aligned} \tag{A16}$$

Therefore,

$$\begin{aligned} v_L(\mathrm{t}) &\approx \sum_{r=1}^{5} K_r \int_0^t a_0 \sin(\omega_r(t-\tau)) \, d\tau \\ &= \sum_{r=1}^{5} \frac{K_r a_0}{\omega_r} (1 - \cos(\omega_r t)) \end{aligned} \tag{A17}$$

Substituting the numerical values of each variable yields:

$$\begin{aligned} v_L(\mathrm{t}) &\approx -0.5322(1 - cos(4.275t)) \\ &+ 0.008(1 - cos(26.791t)) \\ &+ 5.691 \times 10^{-4}(1 - \cos(75.024t)) \\ &- 2.832 \times 10^{-5}(1 - \cos(147.021t)) \\ &+ 2.734 \times 10^{-5}(1 - \cos(243.010t)) \ldots \\ &\approx -0.5322(1 - cos(4.275t))[mm] \end{aligned} \tag{A18}$$